12th International Symposium on Turbulence and Shear Flow Phenomena (TSFP12)
Osaka, Japan (Online), July 19–22, 2022

ASSESSMENT OF THREE WALL MODELS IN A SPATIALLY DEVELOPING THREE-DIMENSIONAL BOUNDARY LAYER IN A BENT SQUARE DUCT

Xiaohan Hu, Imran Hayat, & George Ilhwan Park
Department of Mechanical Engineering and Applied Mechanics
University of Pennsylvania
Philadelphia, Pennsylvania 19104, USA
gipark@seas.upenn.edu

ABSTRACT

We investigate and compare the predictive capabilities of three common wall models in a pressure-driven three-dimensional turbulent boundary layer (3DTBL) developing on the floor of a bent square duct. The wall models employed are a simple equilibrium stress (ODE) model, an integral nonequilibrium wall model, and a PDE nonequilibrium model based on unsteady RANS. The mean flow statistics from WMLES are compared with the experiment of Schwarz & Bradshaw (*J. Fluid Mech.* (1994), vol. 272, pp. 183–210). Although the difference in the wall-stress magnitudes predicted by the three wall models is negligible, the two nonequilibrium wall models are shown to produce a more accurate prediction of the wall-stress direction due to the three-dimensionality incorporated in their formulation, with the PDE nonequilibrium wall model being more accurate among the two. However, the LES solution away from the wall is agnostic to the type of wall model used, resulting in nearly identical predictions of the mean and turbulent statistics in the outer layer for all the wall models. This is explained by the vorticity dynamics and the inviscid skewing mechanism of generating the mean three-dimensionality.

Flow configuration

The reference configuration for the present study is the experimental setup of Schwarz & Bradshaw (1994). In this experiment, a spatially developing turbulent boundary layer grows along the floor of a square duct with a 30° bend (Fig. 1). The boundary layer on the floor was very thin compared to the duct height, with δ_{99}/D ranging between 0.026 and 0.07 throughout the test section, where D is the width (or height) of the square duct. The flow was far from being fully developed. The primary region of interest in the experiment was the centerline region of the duct and it was expected that the secondary flow near the corner regions would have negligible influence on the centerline.

As in the reference study of Schwarz & Bradshaw (1994), the global Cartesian coordinate system is denoted by (x,y,z), whereas a curvilinear coordinate system aligned with the local duct centerline is denoted by (x',y',z'). x' and z' represent the local streamwise and cross-stream directions respectively, and $y = y'$ represents the wall-normal distance from the floor of the duct. In the experiment, the boundary layer on the floor was tripped using a trip wire at the duct inlet located at $x' = 0$. Boundary layers on the other three walls of the duct were not tripped (Schwarz, private communication, 2019). Reynolds number is moderately high, with Re_θ ranging between 4100 and 8500. Upstream of the bend, the flow along the centerline is a canonical 2D zero pressure gradient (ZPG) flat-plate boundary layer. Mean flow three-dimensionality was generated in the bend region approximately between $x' = 1626$ mm and $x' = 2224$ mm due to the cross-stream pressure gradient induced by the bend. Downstream of the bend, the 3DTBL gradually returned to a 2DTBL owing to the vanished spanwise pressure gradient. The experimental study focused on the boundary layer along the local centerline where the streamwise pressure gradient is small.

Fig. 1 shows the test section in the experiment, which consisted of a square duct ($D \times D = 0.762\text{m} \times 0.762\text{m}$) with a total curved length of L = 3.748m. The computational domain is identical to the experimental test section. The present study was conducted at two grid resolutions: a coarse mesh with 8 million control volumes and a fine mesh with 38 million control volumes. The local boundary layer contains approximately 16$\sim$23 and 32$\sim$45 cells across its thickness in the coarse and fine computational meshes, respectively.

Inflow characterization

The experiment reports flow statistics at the 22 locations shown in Fig. 1 along the duct centerline, with the first measurement location being far downstream of the test section inlet (at $x' = 826$ mm). Instead of tripping the boundary layer with a wire as done in the experiment, we employ a synthetic turbulence generator based on a digital filter approach (Klein *et al.*, 2003) for approximating the inflow boundary condition at $x' = 0$ mm. This approach requires iterative guesses on the length of the development region (if any) to be appended upstream of the nominal trip location in the experiment ($x' = 0$ mm), and the state of the inflow to be prescribed at the new inlet location. It should be noted that the goal here is to reproduce the 2DTBL upstream of the bend reasonably well, which then acts as the inflow for the 3DTBL within the bend, rather than to exactly match the flow conditions at the test section inlet. After iterating on several inflow conditions, we found that prescribing a flat-plate turbulent boundary layer at $Re_\theta = 2560$ (Schlatter *et al.*, 2010) at the inlet ($x' = 0$ mm) reproduces the boundary layer statistics well at the first measurement location (station 0: $x' = 826$ mm).Fig. 2 shows reasonable agreement between the simulation and the experiment in terms of the distributions of the boundary layer and momentum thicknesses.

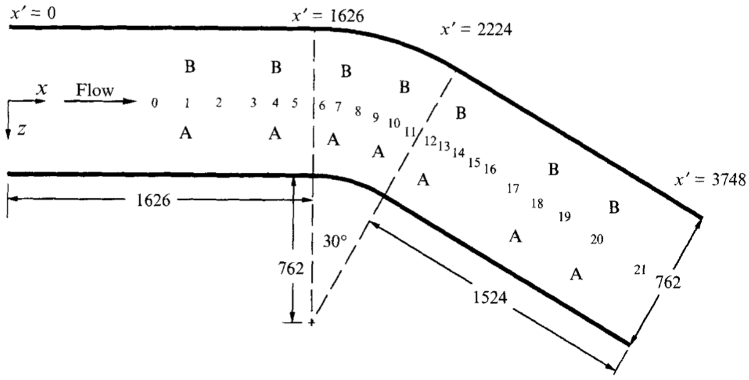

Figure 1. A Schematic of the floor of the duct (reproduction from figure 1 of (Schwarz & Bradshaw, 1994)). The measurement locations in the experiment are marked as numbers 0-21 along the duct centerline. Two coordinate systems are employed. (x, y, z) is a fixed coordinate system with the origin located at the inlet. (x', y', z') is a curvilinear coordinate system aligned with the local duct centerline (measurements in mm).

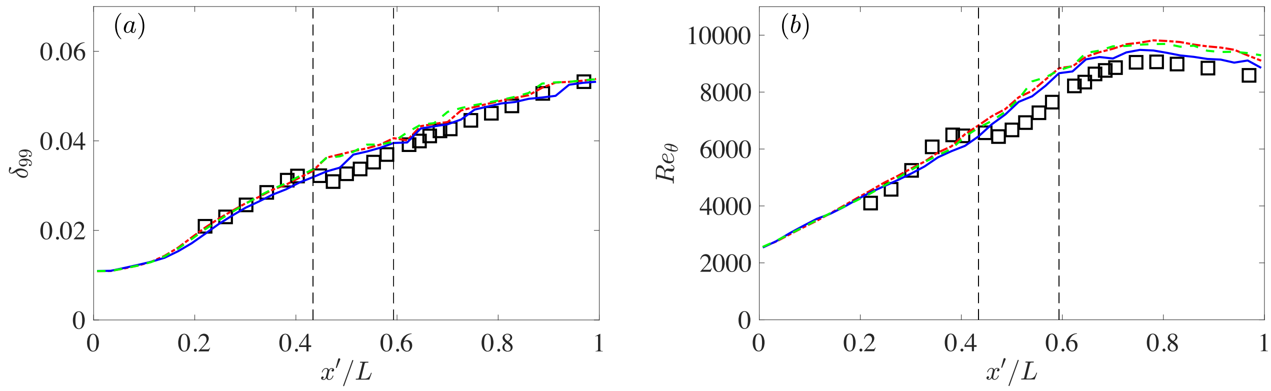

Figure 2. Centerline distributions of (a) boundary layer thickness and (b) momentum thickness (coarse mesh). Symbols, experiment; red dash-dotted line, equilibrium wall model; blue solid line, PDE nonequilibrium wall model; green dashed line, integral nonequilibrium wall model. Black vertical dashed lines denote the start and end of the bend region.

Flow solver and SGS / near-wall modeling

The simulations were performed with CharLES, an unstructured cell-centered finite-volume compressible LES solver developed at Cascade Technologies, Inc. The solver employs an explicit third-order Runge-Kutta (RK3) scheme for time advancement and a second-order central scheme for spatial discretization. The Vreman model (Vreman, 2004) is used to close the SGS stress and heat flux. The three wall models considered in the present study are: an equilibrium stress model (EQWM) in the form of ordinary differential equations (ODE) (Kawai & Larsson (2012)), an integral nonequilibrium wall model (integral NEQWM) that solves the vertically-integrated Navier-Stokes equations with assumed mean velocity profiles for the wall stress, (Yang *et al.* (2015)), and a PDE nonequilibrium wall model (PDE NEQWM) that retains the complexity of the full Navier-Stokes equations (Park & Moin (2014)).

RESULTS

To highlight the characteristics of the 3DTBL, we will focus on the results characterizing the mean flow three-dimensionality here. The variation of the surface flow direction relative to the freestream direction is shown in Fig. 3(a). The flow turning angle is essentially zero in the upstream, grows significantly within the bend, reaches a maximum near the end of the bend, and decays downstream of the bend, though never completely recovering to zero. Consistent with the respective complexity of the three wall models, within the bend region where the 3D effects are most prominent, the PDE NEQWM predicts the flow turning angle most accurately among the three wall models, followed by integral NEQWM, and then EQWM. Fig. 3(b) shows the near-wall flow direction predicted by different wall models through the select surface streamlines calculated from the mean wall shear-stress vector. Although all three wall models predict the flow deviation from the local centerline, the magnitude of deviation is not predicted evenly across the different wall models. This is because the total flow turning is an accumulative effect of the local flow change depicted in Fig. 3(a), and the area under the curve in Fig. 3(a) can be interpreted as an approximation of the near-wall total flow turning angle. Thus, the NEQWM with the highest prediction of local flow angle in the bend shows the largest deviation from the centerline downstream of the bend, even though the local flow angle downstream of the bend is almost equal among the three wall models.

Fig. 4 shows the mean-velocity magnitude profiles for the three wall models, the no-slip simulation and the experiment at several locations along the centerline, including upstream of, within, and downstream of the bend. The no-slip LES with no wall-flux modeling, predicts the mean velocity poorly, highlighting the need for wall modeling for the present flow with the coarse mesh resolution. Here, a higher momentum is imparted to the boundary layer as a consequence of the under-

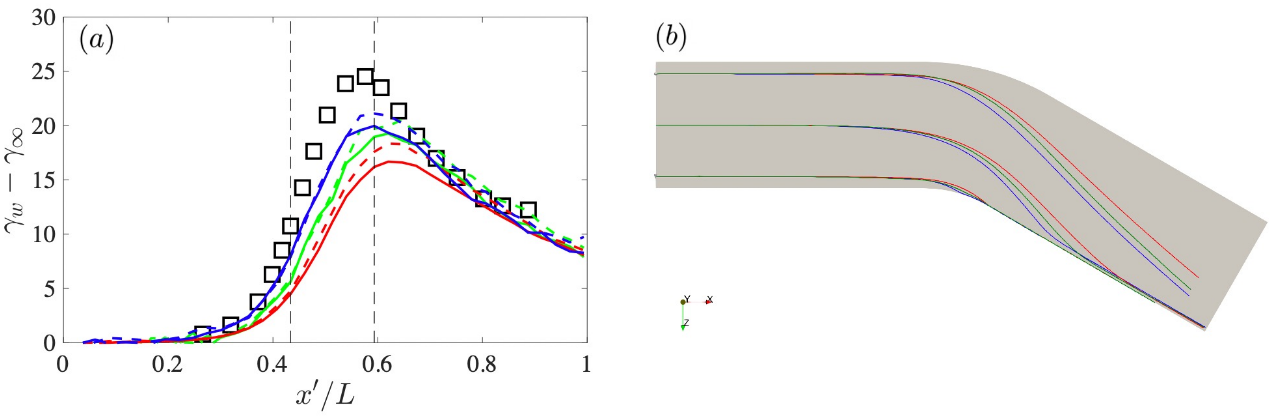

Figure 3. (a) Centerline distribution of surface flow turning-angles with respect to the freestream (γ_w is the wall shear stress direction, γ_∞ is the freestream direction). (b) Streamlines of wall shear stress. Squares: experiment; red line: equilibrium wall model; blue line: PDE nonequilibrium wall model; green line: integral nonequilibrium wall model. Solid line: coarse grid resolution; dashed line: fine grid resolution

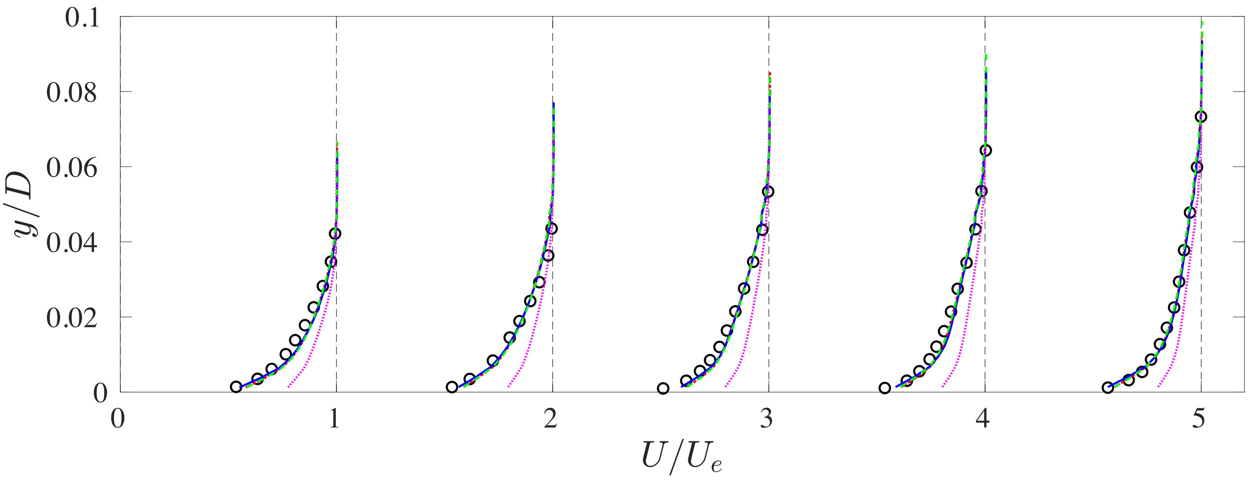

Figure 4. Profiles of the mean-velocity magnitude at 5 measurement locations (stations 4, 8, 12, 16, and 20, from left to right). Station 4 is upstream of the bend; station 8 is within the bend; stations 12, 16 and 20 are downstream of the bend. Red dash-dotted line, EQWM; blue solid line, PDE NEQWM; green dashed line, integral NEQWM; magenta dotted line, no-slip LES; black circle, experiment. Profiles are shifted along the abscissa by 1.

predicted wall shear force. A significant improvement is observed in the predicted mean-velocity profiles with wall modeling. As the predicted skin-friction coefficient magnitude is almost identical from the three wall models (not shown here), we observe very little difference in the mean velocity profiles across the wall models.

To characterize the three-dimensionality of this flow, next we look at the flow direction which is defined by the angle between the mean velocity vector and the freestream velocity vector. Fig. 5 shows the variation in flow direction along the wall-normal direction. The flow direction varies strongly, with the strongest mean flow three-dimensionality observed at the wall, which becomes weaker away from the wall, as evident from the diminishing crossflow away from the wall. A consistent difference of approximately 3 degrees is observed for all three WMLES compared with the experiment, indicating that the difference in the wall-model outputs (the wall-shear force direction observed in Fig. 3(b)) has very little impact on the LES solutions away from the wall.

In this flow, the mean three-dimensionality in the outer layer is created by the inviscid skewing mechanism, where the streamwise vorticity is produced by the reorientation of the spanwise vorticity. We can further analyze the characteristics of such flow from the perspective of the vorticity transport equation. Equation 1 is the transport equation for the mean streamwise vorticity (Bradshaw, 1987), where the terms on the right hand side of this equation represent the contributions from vortex stretching, vortex tilting, Reynolds stress, and viscous effect, in the shown order. The "inviscid skewing" mechanism generates the mean three-dimensionality by reorienting the mean spanwise vorticity as the streamwise vorticity. If we assume that the "inviscid skewing" mechanism is the dominant mechanism for the mean three-dimensionality, the third term on the right hand side would contribute the most to the generation of mean streamwise vorticity. Keeping only the dominant terms in this equation leads to equation 2, where the second equality in this equation is obtained by assuming the mean wall-normal vorticity to be zero ($\Omega_y = \frac{\partial U}{\partial z} - \frac{\partial W}{\partial x} = 0$).

$$U\frac{\partial \Omega_x}{\partial x} + V\frac{\partial \Omega_x}{\partial y} + W\frac{\partial \Omega_x}{\partial z} = \Omega_x \frac{\partial U}{\partial x} + \Omega_y \frac{\partial U}{\partial y} + \Omega_z \frac{\partial U}{\partial z} \quad (1)$$
$$+ \left(\frac{\partial^2}{\partial y^2} - \frac{\partial^2}{\partial z^2}\right)(-\overline{v'w'}) + \frac{\partial^2}{\partial y \partial z}(\overline{v'^2} - \overline{w'^2}) + \nu \nabla^2 \Omega_x$$

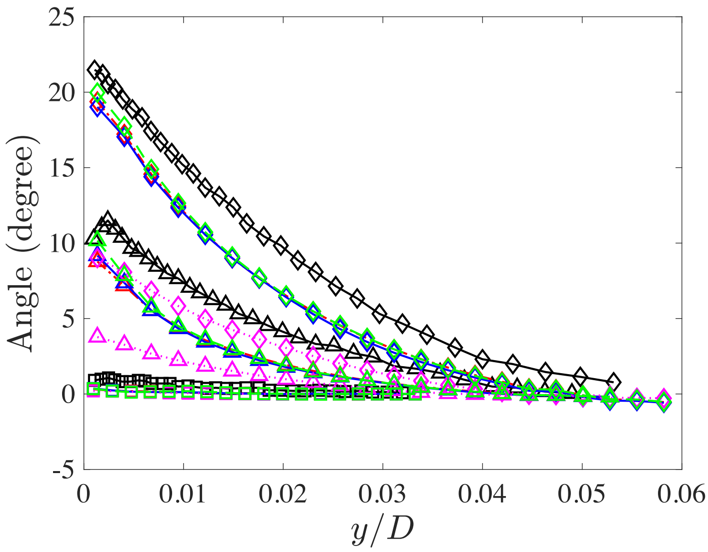

Figure 5. Mean flow direction relative to the local freestream as a function of wall distance. Red dash-dotted line, EQWM; blue solid line, PDE NEQWM; green dashed line, integral NEQWM; magenta dotted line, no-slip LES; black solid line, experiment. Symbols are used to differentiate stations along the duct floor centerline only (Square, station 0; triangle, station 6; diamond, station 10). Lines with the same symbols denote the results at the same stations.

$$U\frac{\partial \Omega_x}{\partial x} = \Omega_z\frac{\partial U}{\partial z} = \Omega_z\frac{\partial W}{\partial x} \tag{2}$$

Reorganizing equation 2 by dividing $U\Omega_z$ gives equation 3. Assuming that Ω_z and U vary little in the streamwise direction, we can re-express this equation as equation 4.

$$\frac{1}{\Omega_z}\frac{\partial \Omega_x}{\partial x} = \frac{1}{U}\frac{\partial W}{\partial x} \tag{3}$$

$$\frac{\partial}{\partial x}\frac{\Omega_x}{\Omega_z} = \frac{\partial}{\partial x}\frac{W}{U} \tag{4}$$

Equation 4 is referred to as the SWH relation in the global coordinate system. Equation 2 in the local freestream coordinate system is given by equation 5 Horlock & Lakshminarayana (1973):

$$U_s\frac{\partial \Omega_s}{\partial s} + \frac{U_s\Omega_n}{R} = \Omega_s\frac{\partial U_s}{\partial s} + \Omega_n\frac{\partial U_s}{\partial n} + \Omega_b\frac{\partial U_s}{\partial b}, \tag{5}$$

here, $(s,\ n,\ b)$ represents the streamwise, spanwise and wall normal directions in the local freestream coordinate system, respectively. Since $\Omega_n = \frac{\partial U_s}{\partial b}$ and $\Omega_b = -(\frac{\partial U_s}{\partial n} + \frac{U_s}{R})$, we get,

$$\frac{\partial}{\partial s}\left(\frac{\Omega_s}{U_s}\right) = -\frac{2\Omega_n}{U_s R} \tag{6}$$

Using the relation $Rd\theta = ds$, equation 6 can be re-written as equation 7, which is the SWH formula in the local freestream coordinate system.

$$\frac{d\Omega_s}{\Omega_n} = -2d\theta. \tag{7}$$

Integrating equation 7 along the streamline and substituting the definitions of vorticity, we get,

$$\frac{U_n}{U_e} = 2\gamma_e\left(1 - \frac{U_s}{U_e}\right). \tag{8}$$

When the "inviscid skewing" mechanism is the dominant generation mechanism of the mean streamwise vorticity (mean three-dimensionality), U_n plotted against U_s under the local freestream coordinates will form a straight line. Fig. 6 shows the Johnston triangular plot for the current flow in bent duct and a temporally developing shear-driven 3D channel flow from Lozano-Durán *et al.* (2020). It is observed that the mean velocities in the outer layer from the duct flow satisfy the SWH formula well, whereas they deviate from the SWH relation in the shear-driven case. This indicates the "inviscid skewing" mechanism is the dominant contribution to the mean three-dimensionality in the outer part of the boundary layer in the duct flow. While in the transient 3D channel flow, "inviscid skewing" does not exist, i.e. the vortex tilting term is zero, as expected. The slope in the SWH relation represents the freestream turning angle with respect to the upstream flow, and the freestream slope in the triangular plot (Fig. 6(*a*)) therefore increases toward the downstream direction.

In addition to the LES solution, Fig. 7 also shows the wall-model solutions (i.e. the mean velocities solved within the wall-models) in the triangular plot. It shows that different wall models have different capabilities in predicting the skewed mean-velocity profiles. The wall model solutions are plotted from the origin to the LES matching locations. The EQWM, due to its unidirectional-flow assumption, cannot describe skewed mean-velocity profiles. It shows up as a straight line starting from the origin in the triangular plot. For PDE NEQWM and integral NEQWM, the profiles appear as curved lines in the triangular plot, which means the flow direction changes with the wall distance. Thus, the two NEQWM are able to capture the skewed mean-velocity profiles. At station 8 where the three dimensionality is strongest, the PDE NEQWM is able to express a richer wall-normal dependent skewness

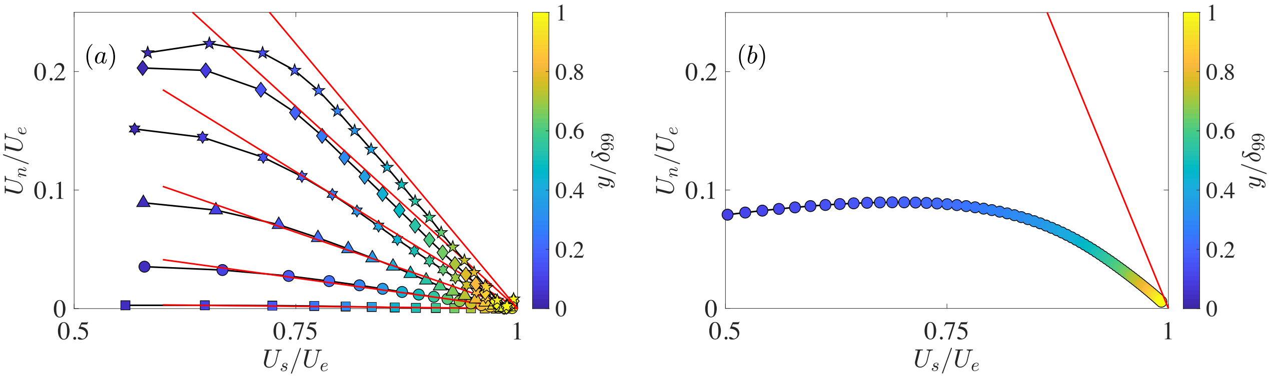

Figure 6. Johnston triangular plot (a) WMLES (EQWM) of the bent square duct: square, station 0; circle, station 4; triangle, station 6; cross, station 8; diamond, station 10; star, station 12. (b) DNS of the shear-driven 3DTBL from the transient channel flow at $Re_\tau = 546$ at $t^+ = 192$ (Lozano-Durán *et al.*, 2020). Red straight line, the SWH formula Eq. (8). Color bar denotes the wall distance normalized by the local boundary layer thickness.

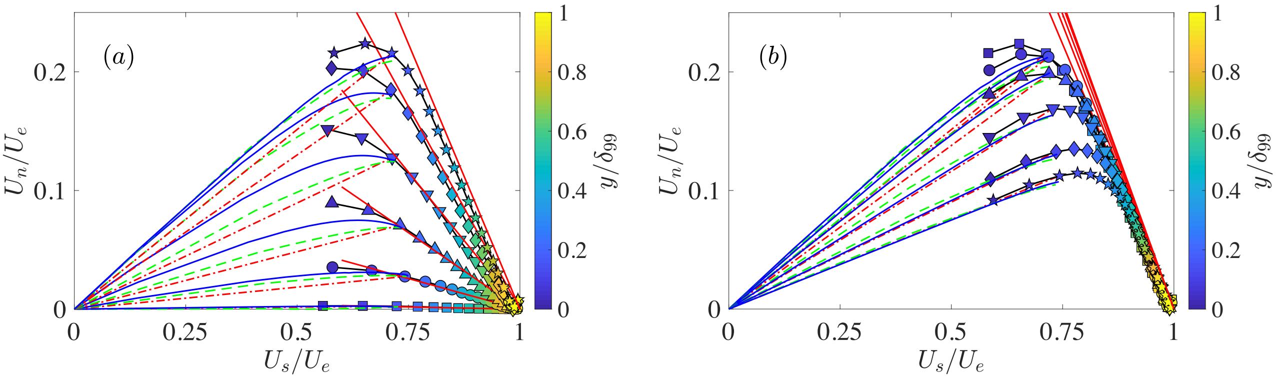

Figure 7. Johnston triangular plot of the WM and LES solutions. The outer layer LES solution, which predicted almost identically with different wall models, is colored by the wall distance normalized by the local boundary layer thickness. (a) Crossflow developing stage: square, station 0; circle, station 4; upward-pointing triangle, station 6; downward-pointing triangle, station 8; diamond, station 10; star, station 12. (b) Crossflow decaying stage: square, station 12; circle, station 14; upward-pointing triangle, station 16; downward-pointing triangle, station 18; diamond, station 20; star, station 21. Red solid straight lines from the bottom right corner are given by the SWH formula Eq.(8). Red dash-dotted lines from the origin represent the wall-model solution: EQWM; blue solid line: PDE NEQWM; green dashed line: integral NEQWM.

than the integral NEQWM. During the crossflow developing stage (Fig. 7(a)), the difference between the two NEQWM solutions and the EQWM solution gradually grows. Downstream of the bend, where the crossflow starts to decay (Fig. 7(b)), the triangular plots for the three wall model solutions progressively collapse onto each other, until they become almost identical toward the end of the duct, where the flow is essentially unidirectional.

REFERENCES

Bradshaw, P. 1987 Turbulent secondary flows. Ann. Rev. Fluid Mech. **19**, 53–74.

Horlock, J. H. & Lakshminarayana, B. 1973 Secondary flows: theory, experiment, and application in turbomachinery aerodynamics. Ann. Rev. Fluid Mech. **5**, 247–280.

Kawai, S. & Larsson, J. 2012 Wall-modeling in large eddy simulation: Length scales, grid resolution, and accuracy. Phys. Fluids **24**, 015105.

Klein, M., Sadiki, A. & Janicka, J. 2003 A digital filter based generation of inflow data for spatially developing direct numerical or large eddy simulations. J. Comput. Phys. **186**, 652–665.

Lozano-Durán, A., Giometto, M. G., Park, G. I. & Moin, P. 2020 Non-equilibrium three-dimensional boundary layers at moderate reynolds numbers. J. Fluid Mech. **883**, A20.

Park, G. I. & Moin, P. 2014 An improved dynamic non-equilibrium wall-model for large eddy simulation. Phys. Fluids **26**, 015108.

Schlatter, P., Li, Q., Brethouwer, G., Johansson, A. V. & Henningson, D. S. 2010 Simulations of spatially evolving turbulent boundary layers up to $re_\theta = 4300$. Int. J. Heat. Fluid. Fl. **31**, 251–261.

Schwarz, W. R. & Bradshaw, P. 1994 Turbulence structural changes for a three-dimensional turbulent boundary layer in a 30 ° bend. J. Fluid Mech. **272**, 183–210.

Vreman, A. W. 2004 An eddy-viscosity subgrid-scale model for turbulent shear flow: Algebraic theory and applications. Phys. Fluids **16**, 3670.

Yang, X. I. A., Sadique, J., Mittal, R. & Meneveau, C. 2015 Integral wall model for large eddy simulations of wall-bounded turbulent flows. Phys. Fluids **27**, 025112.